

Theoretical Insights into the Enantioselectivity and Mechanism of Diels–Alder Reactions Involving Chiral Cationic Oxazaborolidinium Catalyst

Nasr Y. M. Omar, Noorsaadah A. Rahman, and Sharifuddin Md Zain*

Department of Chemistry, University of Malaya, 50603 Kuala Lumpur, Malaysia

Received August 30, 2010; E-mail: smzain@um.edu.my

The chiral oxazaborolidinium ion catalyzed Diels–Alder reaction between 2-methyl-1,3-butadiene and 2,3-dimethyl-1,4-benzoquinone was studied by means of density functional theory (DFT) at the B3LYP/6-31G(d) level of theory. Different DFT-based theoretical approaches including the reaction force, the natural population analysis of the charge transfer, the topological analysis of the electron localization function (ELF), and the global and local reactivity indices were applied to investigate and rationalize the mechanism and the *endo*/*exo* selectivity of this reaction. The changes in the physical and chemical properties of the reacting molecules along the intrinsic reaction coordinate (IRC) were also monitored to shed light on the mechanistic details. The analysis of the studied Diels–Alder reaction within the framework of DFT revealed and explained the preference of the *endo* path to the *exo* channel, and pointed out a concerted but highly asynchronous reaction mechanism.

The Diels–Alder cycloaddition reaction is one of the most powerful reactions for the construction of six-membered rings with several stereogenic centers in a regio- and stereo-controlled way. In this reaction, a molecule with a conjugated system of four π electrons (the diene) reacts with another molecule with two π electrons (the dienophile) to produce a molecule with a six-membered ring by the formation of two new σ bonds. The nature of the formation of these new σ bonds has been the subject of long debate.[1–5] Two mechanisms are possible; a concerted mechanism involving a partial formation of the two new σ bonds in a single transition structure, and a stepwise mechanism having a zwitterionic or biradical intermediate with one of the σ bonds formed. In the concerted mechanism, if the two σ bonds are formed to the same extent, then the reaction is synchronous. Otherwise, it is asynchronous.

The development of enantioselective Diels–Alder reactions utilizing chiral organocatalysts has been the subject of numerous studies.[6–16] For instance, the chiral cationic oxazaborolidinium catalyst **1** (Chart 1) has been shown to be a very versatile and powerful catalyst for the synthesis of many biologically complex molecules such as estrone, the oral contraceptive desogestrel, and the antiflu drug oseltamivir.[8]

The Diels–Alder reaction of quinones is highly useful in the synthesis of many complex natural products. An example of an enantioselective Diels–Alder reaction involving the chiral cationic oxazaborolidinium catalyst **1** has been shown by Corey in a reaction between 2-methyl-1,3-butadiene (isoprene) (**2**) and 2,3-dimethyl-1,4-benzoquinone (**3**)[8,11] and is shown in Scheme 1 (Reaction 1).

The Diels–Alder reaction, in terms of the nature of the interaction between the diene and the dienophile as well as the selectivity, mechanism, and progress of the reaction, has been studied through various theoretical approaches. These include: (1) frontier molecular orbital (FMO) analysis,[17–19] (2) bond order analysis, natural bond orbital (NBO) methods, and topological analysis of the electron localization function (ELF),[20–26] (3) global and local reactivity descriptors,[27–31] (4)

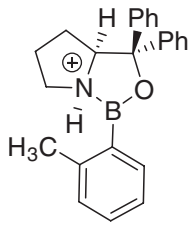

1

Chart 1.

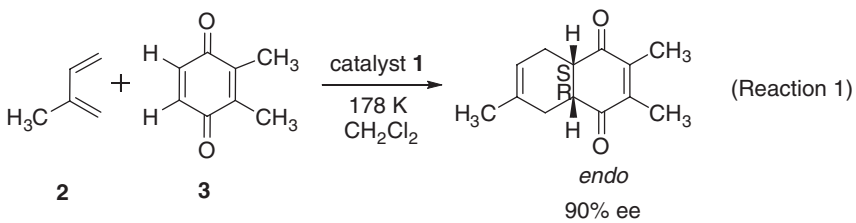

2 **3**

Scheme 1. Corey's enantioselective Diels–Alder reaction of benzoquinone using chiral oxazaborolidinium catalyst.[11]

Published on the web February 4, 2011; doi:10.1246/bcsj.20100242

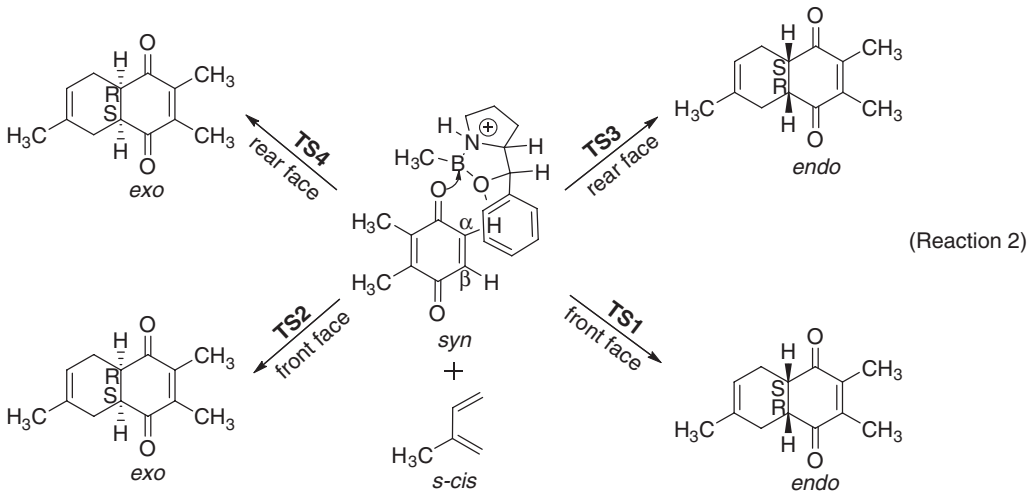

Scheme 2. Catalyzed Diels–Alder reaction with four possible reaction pathways. The catalyst is coordinated *syn* to the HC=CH double bond that undergoes the [4 + 2]-cycloaddition. The addition of the diene is either to the front face of the α,β double bond (i.e., away from the phenyl group of the catalyst) or to the rear face of the α,β double bond. Transition states are as shown in Figure 2.

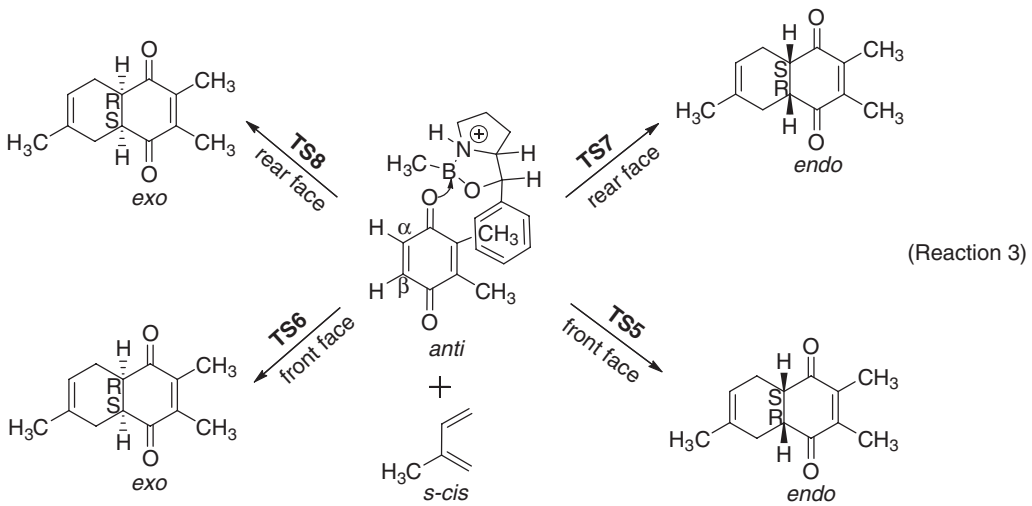

Scheme 3. Catalyzed Diels–Alder reaction with four possible reaction pathways. The catalyst is coordinated *anti* to the HC=CH double bond that undergoes the [4 + 2]-cycloaddition. The addition of the diene is either to the front face of the α,β double bond (i.e., away from the phenyl group of the catalyst) or to the rear face of the α,β double bond. Transition states are as shown in Figure 3.

reaction path and reaction force analysis,[32] and (5) aromaticity.[33,34] However, to the best of our knowledge, these DFT-based approaches have not been used for the description of enantioselective organocatalytic Diels–Alder reactions.

The objective of the present study is to examine the applicability of a number of these theoretical approaches to investigate and rationalize the mechanism and enantioselectivity of the organocatalytic Diels–Alder reaction. The reaction studied is between 2-methyl-1,3-butadiene (**2**) and 2,3-dimethyl-1,4-benzoquinone (**3**) in the presence of model catalyst **4** (Chart 2 and Schemes 2 and 3).[35] It is hopeful that the outcome of this work will aid in deeper understanding of the mechanism and enantioselectivity of organocatalytic Diels–Alder reactions.

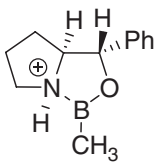

4

Chart 2.

Computational Methods

All DFT calculations were carried out in vacuo at the B3LYP/6-31G(d) level of theory as implemented in the Gaussian 03 program.[36] Geometry optimizations to local minima and transition structures were accomplished with the Berny algorithm in redundant internal coordinates without any symmetry restriction. Vibrational frequency calculations were performed at the optimized geometries to verify whether the

obtained structures are minima or transition structures as well as to determine zero-point vibrational energies and thermochemical quantities. The vibration associated with the imaginary frequency was ensured to correspond to a displacement in the direction of the reaction coordinate. The zero-point vibrational energies and thermochemical quantities were calculated using frequencies scaled by 0.9804. Thermochemical quantities were calculated at 178 K and at 1.0 atm pressure.

All atomic charges were obtained from natural population analysis (NPA)[37,38] at the same level of theory using the NBO program integrated into Gaussian 03. The reaction forces were obtained by tracing the intrinsic reaction coordinate (IRC)[39–41] as implemented in Gaussian 03 using the same calculation level. A total of 40 points were examined along the reaction path (both the forward and the backward directions) with a default step size of 0.1 amu$^{1/2}$ Bohr. Electron localization function (ELF)[24,42–45] calculations were performed for the reactants, products, transition structures, and critical points along the IRC path using the DGrid program.[46] The Mayer bond orders[47–50] were calculated for the reactants, products, transition structures and critical points along the IRC path using the EFF-AO program.[51] This was achieved by performing single-point HF/STO-3G calculations at the B3LYP/6-31G(d) optimized structures using the Gaussian 03 program. The Gaussian formatted checkpoint file is then used by the EFF-AO program for bond order analysis. The use of the minimal STO-3G basis set is recommended for bond order and valence indices analysis and gives the most reliable values.[52–54]

Global reactivity indices including electronic chemical potential (μ), chemical hardness (η), electrophilicity (ω), and nucleophilicity (N) are calculated as follows:[55–57]

$$\mu \approx \frac{1}{2}(\varepsilon_H + \varepsilon_L) \quad (1)$$

$$\eta \approx \varepsilon_L - \varepsilon_H \quad (2)$$

$$\omega = \frac{\mu^2}{2\eta} \quad (3)$$

$$N = \varepsilon_{H(Nu)} - \varepsilon_{H(tetracyanoethylene)} \quad (4)$$

where ε_H and ε_L are the one-electron energies of the HOMO and the LUMO, respectively. The local electrophilicity index[56,58] (ω_k) and the local nucleophilicity index[59] (N_k) are calculated as

$$\omega_k = \omega f_k^+ \quad (5)$$

$$N_k = N f_k^- \quad (6)$$

where f_k^+ and f_k^- are the condensed Fukui functions for nucleophilic and electrophilic attacks, respectively.

Results and Discussion

Geometries and Energetics of the Transition States. The B3LYP/6-31G(d) optimized structures of the *syn*-**R1** and *anti*-**R2** coordination complexes between benzoquinone **3** and catalyst **4** are illustrated in Figure 1. A stronger coordination is observed for the *syn*-complex having a B–O bond length shorter by 0.06 Å than that of the *anti*-complex. In addition, the *syn*-complex shows a nonconventional hydrogen bond[60,61] between the C_α–H hydrogen and the catalyst oxygen with 2.27 Å bond length.

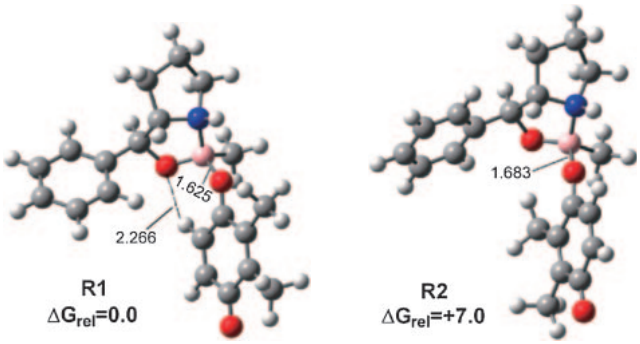

Figure 1. Reactant B3LYP/6-31G(d) optimized structures. Relative free energies are in kcal mol^{-1} at 178 K. Distances are in angstroms. Color code: carbon in gray, hydrogen in white, oxygen in red, nitrogen in blue, and boron in pink.

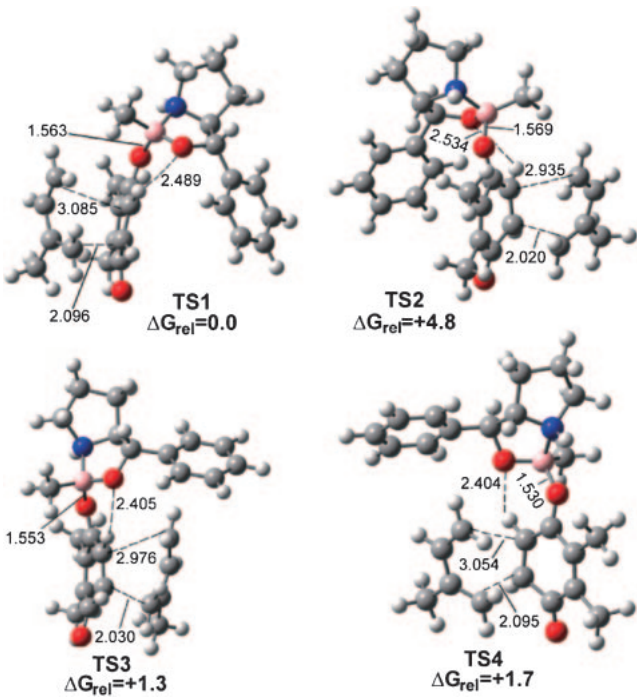

Figure 2. B3LYP/6-31G(d) optimized transition structures for Reaction (2). Relative free energies are in kcal mol^{-1} at 178 K. Distances are in angstroms. **TS1**: *endo* transition state involving diene attack to the front face, **TS2**: *exo* transition state involving diene attack to the front face, **TS3**: *endo* transition state involving diene attack to the rear face, and **TS4**: *exo* transition state involving diene attack to the rear face. The color code is the same as in Figure 1.

The B3LYP/6-31G(d) computed transition structures for Reactions (2) and (3) are shown in Figures 2 and 3, respectively. The *syn* transition structures (Figure 2) are more stable than their *anti*-counterparts (Figure 3) by about 3.4 to 9.4 kcal mol^{-1}. For both *syn* and *anti* transition structures, the B–O bond length is shorter (on average) than that of the reactant by 0.07 and 0.11 Å, respectively indicating stronger complexation at the transition state. A relatively stronger coordination is observed for the *syn* transition structures with B–O bond lengths shorter by about 0.01 to 0.04 Å than those of the *anti* transition structures. Similar to the reactants, the *syn*

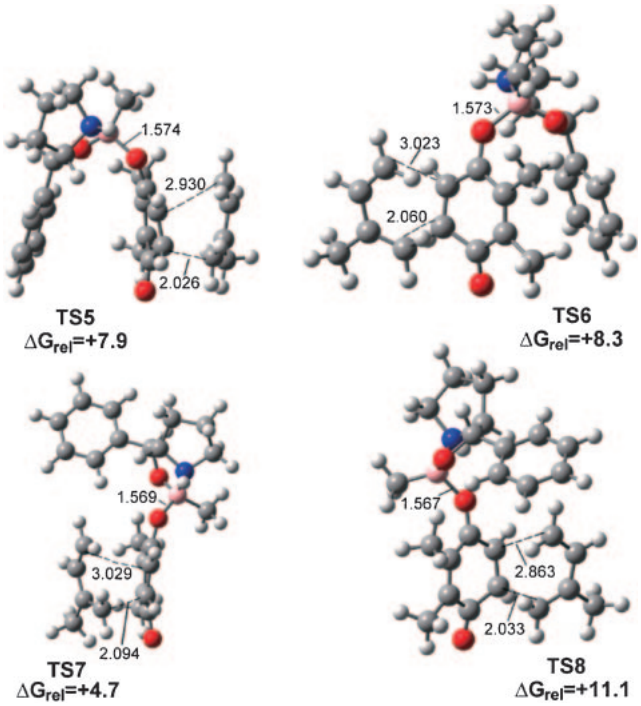

Figure 3. B3LYP/6-31G(d) optimized transition structures for Reaction (3). Relative free energies are in kcal mol^{-1} at 178 K. These energies are relative to **TS1**. Distances are in angstroms. **TS5**: *endo* transition state involving diene attack to the front face, **TS6**: *exo* transition state involving diene attack to the front face, **TS7**: *endo* transition state involving diene attack to the rear face, and **TS8**: *exo* transition state involving diene attack to the rear face. The color code is the same as in Figure 1.

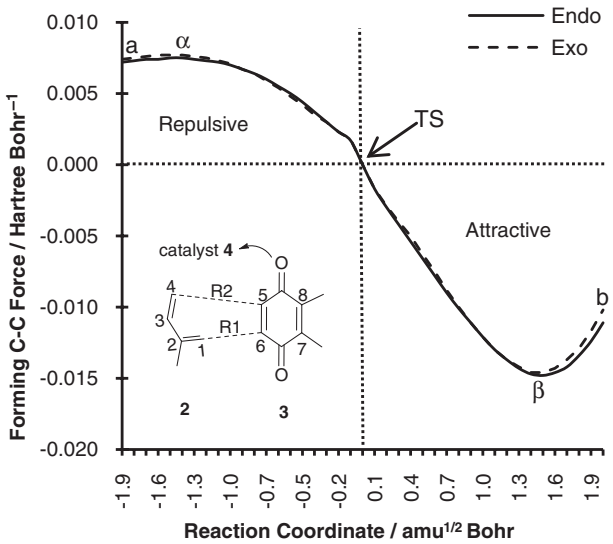

Figure 4. Reaction force profiles associated with the internal coordinate **R1** for the *endo* and the *exo* channels of the Diels–Alder reaction between **2** and **3** in the presence of catalyst **4**. Points α, TS, and β are described in the text. Point a is the last point examined along the path in the backward (reactants) direction. Point b is the last point examined along the path in the forward (product) direction.

transition structures have a nonconventional hydrogen bond between the C_α–H hydrogen and the catalyst oxygen with bond lengths in the range of 2.40–2.53 Å.

For the *endo* transition states, the lowest energy transition state is **TS1** representing ≈97.55% of the Boltzmann population of the *endo* transition states. As for the *exo* transition states, **TS4** represents the most stable transition state with ≈99.98% of the Boltzmann population of the *exo* transition states. The percent enantiomeric excess (%ee) is calculated to be 98.3% at 178 K favoring the *endo*-product.

The degree of asynchronicity is the difference between the lengths of the two forming C–C bonds at the transition structure. In the present study, the average degree of asynchronicity for the transition structures is calculated to be 0.93 Å (Figures 2 and 3). Thus, these transition structures point to concerted but highly asynchronous reaction pathways where the bond between the diene and carbon β of the dienophile is being formed in a larger extent than the bond between the diene and carbon α of the dienophile.

In the sections to follow, only the most energetically favorable transition states for the *endo* (**TS1**) and the *exo* (**TS4**) channels will be discussed.

Reaction Force Analysis along the Intrinsic Reaction Coordinate. During a chemical reaction, the changes in the physical and chemical properties of the reaction complex (i.e., the reacting molecules) along the IRC can be investigated to gain insights into the reaction mechanism. The motion of the reaction complex across the IRC is a direct result of the forces exerted on its atoms. The reaction forces associated with the internal coordinate **R1** (i.e., the coordinate that corresponds to the forming carbon–carbon bond) along the IRC are illustrated in Figure 4 for both *endo* and *exo* routes. The total reaction forces along the IRC for both *endo* and *exo* channels are represented in Figure 5. As can be seen from Figures 4 and 5, the reaction force profile possesses three key points along the IRC, namely, α, TS and β. For both *endo* and *exo* channels, monitoring the internal coordinate **R1** along the IRC shows that the repulsive force starts to diminish at point α where the **R1** value is 2.38 Å. At this distance, the overlap between π-orbitals is ≈0.02 Å[32] which marks the start of the attractive force. The attractive force persists until point β where the **R1** value is 1.82 Å. At this point, the final stage for the formation of the carbon–carbon single bond begins.

Both Figures 4 and 5 show the *endo* route to have less repulsive forces than the *exo* path. This leads to a lowering of the reaction barrier (i.e., the activation energy) for the *endo* channel rendering it the kinetically preferred path for this reaction. In addition, after point β toward the products, the attractive forces due to carbon–carbon single bond formation become more evident for the *endo* path. Again, this reflects that the formation of the *endo* product is favored over the *exo* one.

Natural Population Analysis (NPA). Natural population analysis offers a tool for evaluating the charge transfer (CT) along the reaction path. The charge transferred from diene **2** to dienophile **3** along the IRC is given in Table 1. As can be deduced from the table, the charge transfer associated with the more favorable *endo* path is larger than that associated with the *exo* route. This larger charge transfer leads to a lower exchange (or Pauli) repulsion (smaller repulsive forces (Figures 4 and 5))

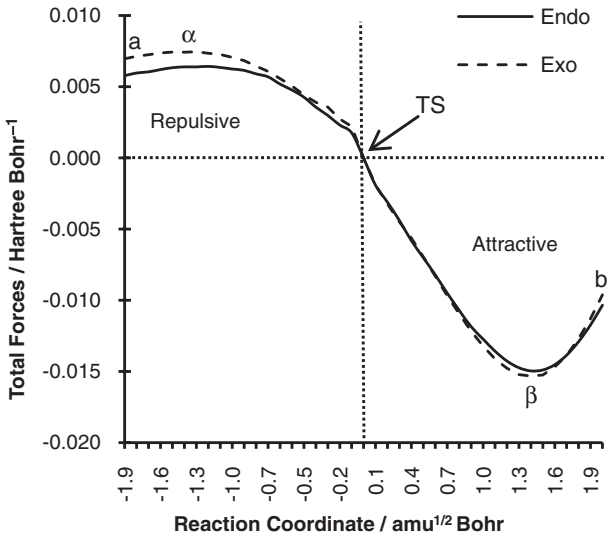

Figure 5. Reaction force profiles associated with all Cartesian coordinates for the *endo* and the *exo* channels of the Diels–Alder reaction between **2** and **3** in the presence of catalyst **4**. Points α, TS, and β are described in the text. Point a is the last point examined along the path in the backward (reactants) direction. Point b is the last point examined along the path in the forward (product) direction.

Table 1. Natural Population Analysis of the Charge (e) Transferred from **2** to **3** along the IRC[a)]

	CT
endo path	
Point (a)	0.293
Point (α)	0.293
TS	0.294
Point (β)	0.294
Point (b)	0.295
exo path	
Point (a)	0.154
Point (α)	0.189
TS	0.220
Point (β)	0.268
Point (b)	0.278

a) Points are as illustrated in Figures 4 and 5.

and hence is responsible for the lower activation energy of the *endo* channel.[32] In addition, the progress of the charge transfer along the IRC is much faster for the *endo* channel than that of the *exo* route, and is almost completed at the transition state (Table 1). This again leads to a lower barrier and more stabilization for the *endo* route. For both the *endo* and *exo* paths, point b on the IRC marks the end of charge transfer. At this point, the total amount of charge transferred from diene **2** to dienophile **3** is 0.30 e and 0.28 e for the *endo* and the *exo* channels, respectively (Table 1), indicating a more polar character for the *endo* route.

Topological Analysis of the Electron Localization Function. The electron localization function (ELF)[24,42,44,45] aids in understanding the concept of electron pair localization (core, lone pair and bonding electrons) that corresponds to Lewis structures, which in turn helps in the rationalization and understanding of the molecular structure, bonding, chemical reactivity, and reaction mechanism.[20–23]

Table 2. Electron Populations for the Valence ELF Basins of the Reacting Complex **2**–**3**–**4** along the IRC[a)]

	$V_{1+2}(C_1,C_2)$	$V_1(C_2,C_3)$	$V_{1+2}(C_3,C_4)$	$V_{1+2}(C_5,C_6)$	$V_1(C_1,C_6)$
endo path					
Point (a)	3.64	1.89	3.55	3.66	—
Point (α)	3.63	1.89	3.55	3.66	—
TS	3.58	1.89	3.55	3.63	—
Point (β)	**1.86**	1.90	3.54	**1.80**	**1.73**
Point (b)	**1.86**	1.90	3.55	**1.81**	**1.77**
exo path					
Point (a)	3.64	1.90	3.56	3.66	—
Point (α)	3.63	1.90	3.55	3.65	—
TS	3.59	1.90	3.56	3.64	—
Point (β)	**1.86**	1.89	3.57	**1.79**	**1.74**
Point (b)	**1.86**	1.89	3.58	**1.80**	**1.78**

a) V_1 represents one disynaptic basin and V_{1+2} represents the combination of two disynaptic basins. Points and carbon numbers are as illustrated in Figure 4.

The topological analysis of the ELF gradient field allows partitioning of the molecular space into basins of attractors (maxima) that correspond to the bonds and lone pairs in the Lewis structure model.[24,45] There are two types of basins:[24,45] a core basin (C) that contains a nucleus (except a proton) and a valence basin (V) that lacks nucleus and is always connected with one or more core basins. A monosynaptic basin is connected with only one core basin and corresponds to a lone pair. A disynaptic basin is connected with two core basins and represents a two-center covalent bond. Integrating the electron density over the basin volume produces the basin population.

The topology of the ELF of the reacting complex (the diene **2**, the dienophile **3**, and the catalyst **4**) is analyzed in order to gain insights into the electron density evolution along the IRC. This corresponds to the breaking and formation of the carbon–carbon double bonds along the IRC. The electron populations of the more relevant valence basins are listed in Table 2. In the case of carbon–carbon double bonds, the electron population is given as the sum of the two individual electron populations associated with the two disynaptic basins used to describe the double bond.

For both *endo* and *exo* channels, the most noticeable changes in the electron population along the IRC are observed at point β (Table 2). At this point, the two disynaptic basins $V_{i=1,2}(C_1,C_2)$ found at the preceding points are merged into one disynaptic basin $V_1(C_1,C_2)$ with an electron population of 1.86 e. This indicates the transformation of $C_1{=}C_2$ double bond of the diene into C_1–C_2 single bond. Similarly, the two disynaptic basins $V_{i=1,2}(C_5,C_6)$ found at the preceding points are fused into one disynaptic basin $V_1(C_5,C_6)$ with an electron population of 1.80 e pointing out the transformation of $C_5{=}C_6$ double bond of the dienophile into C_5–C_6 single bond. In addition, one new disynaptic basin $V_1(C_1,C_6)$ with an electron population of 1.73 e is created which indicates that the formation of C_1–C_6 single bond is in its final stage (the electron population of the disynaptic basin $V_1(C_1,C_6)$ is 1.82 e

Table 3. Computed Mayer Bond Orders, BO, for the Reacting Complex **2**–**3**–**4** along the IRC[a)]

	BO_{1-2}	BO_{2-3}	BO_{3-4}	BO_{4-5}	BO_{5-6}	BO_{1-6}
endo path						
Point (a)	1.787	1.079	1.887	0.012	1.701	0.073
	[1.368]	[1.456]	[1.350]	[3.210]	[1.365]	[2.449]
Point (α)	1.734	1.093	1.870	0.018	1.645	0.118
	[1.375]	[1.451]	[1.351]	[3.165]	[1.373]	[2.334]
TS	1.535	1.149	1.807	0.040	1.446	0.309
	[1.399]	[1.437]	[1.357]	[3.085]	[1.399]	[2.096]
Point (β)	1.222	1.265	1.683	0.074	1.169	0.663
	[1.443]	[1.418]	[1.366]	[3.010]	[1.442]	[1.820]
Point (b)	1.138	1.311	1.635	0.087	1.103	0.770
	[1.462]	[1.411]	[1.370]	[2.960]	[1.459]	[1.714]
exo path						
Point (a)	1.790	1.076	1.893	0.014	1.683	0.076
	[1.366]	[1.456]	[1.349]	[3.164]	[1.369]	[2.455]
Point (α)	1.740	1.089	1.878	0.019	1.628	0.119
	[1.372]	[1.451]	[1.350]	[3.127]	[1.377]	[2.347]
TS	1.528	1.146	1.812	0.040	1.414	0.324
	[1.395]	[1.437]	[1.356]	[3.054]	[1.404]	[2.095]
Point (β)	1.217	1.261	1.688	0.065	1.147	0.674
	[1.437]	[1.418]	[1.366]	[2.980]	[1.448]	[1.812]
Point (b)	1.136	1.307	1.639	0.074	1.087	0.778
	[1.454]	[1.410]	[1.371]	[2.930]	[1.465]	[1.704]

a) The corresponding bond lengths (Å) are given in brackets. Points and carbon numbers are as illustrated in Figure 4.

for the products). The flow of the electron density to the newly created basin is continued and the formation of C_1–C_6 single bond is complete after point b. The topological analysis of the ELF however, did not provide any sign regarding the formation of C_4–C_5 single bond and the formation of C_2=C_3 double bond. This might be due to the high asynchronous nature of the studied reaction. As observed in Table 2, both *endo* and *exo* channels show the same trend with almost identical basin populations. Hence, it was not possible to investigate the *endo*/*exo* selectivity based on the topological analysis of the ELF.

Bond Order Analysis. The extent of the bond breaking/forming along the IRC for both *endo* and *exo* channels as assessed by the use of Mayer bond order is given in Table 3. The associated bond lengths are also provided in the table. As is displayed in Table 3, the transformation of C_1=C_2 and C_5=C_6 double bonds into the corresponding single bonds is more evident and is more advanced than the transformation of C_3=C_4 double bond consistent with the results obtained from the topological analysis of the ELF (the above section). In addition, the bond order analysis shows that the formation of C_2=C_3 double bond is progressing although at a slower rate than the break of the C_1=C_2 and C_5=C_6 double bonds. Moreover, the formation of C_1–C_6 single bond is observed to progress faster than the formation of C_4–C_5 single bond indicating a highly asynchronous bond formation. This is consistent with the topological analysis of the ELF (the above section). Furthermore, at point b on the IRC, the bond order analysis revealed the formation of C_1–C_6 single bond to be at a very advanced stage.

The electrostatic contribution to the diatomic interaction energy in the energy decomposition scheme proposed by Mayer[48,50,62] provides a link between the bond order and the diatomic energy. In a point-charge approximation, the electrostatic interaction energy is given by[48,50,62]

$$E_{A-B}^{\text{point}} = \frac{1}{R_{A-B}}\left(q_A q_B - \frac{1}{2}\text{BO}_{A-B}\right) \quad (7)$$

where R_{A-B} is the distance between atoms A and B, and q is the Mulliken atomic charge. In addition to the classical electrostatic interaction, eq 7 includes a nonclassical exchange repulsion energy contribution that is related to the bond order.[48,50,62]

To investigate the influence of the bond breaking/forming on the diatomic energy in terms of the electrostatic and exchange interactions, eq 7 is applied for each atomic pair involved in the reaction. The results are tabulated in Table 4. The relative energy in units of kcal mol^{-1} for each point along the IRC is also listed in the table. From Table 4, in terms of the electrostatic and exchange interactions, the break of C_1=C_2, C_3=C_4, and C_5=C_6 double bonds is repulsive and destabilizing while the formation of C_1–C_6 and C_4–C_5 single bonds, and C_2=C_3 double bond is attractive and stabilizing. Based on the total energy of these interactions, the *endo* channel is more stable than the *exo* path at points α, TS, and β with the stabilization in the energy being more evident at point α and at the transition state (2.13 and 1.11 kcal mol^{-1}, respectively, Table 4). These results describe, in part, the preference of the *endo* channel over the *exo* route in the studied reaction. However, it should be pointed out that the *exo* route is slightly more stable than the *endo* path at points a and b (Table 4).

The final issue regarding the structural parameters to comment about is the boron–oxygen bond length along the IRC. It is observed that the length of this bond is not only shortened in going from the reactants to the transition state structure but also from the transition state structure to the final point examined on the IRC (i.e., point b) (the B–O bond length at this point is found to be 1.55 Å). This is in line with Corey's prediction which stated,[13] "It is important to note in this context that the coordination of catalyst to the carbonyl persists not only in the transition state but even in the Diels–Alder adduct."

Analysis of the Global and Local Reactivity Indices. The chemical reactivity indices provide useful tools to examine the polar character of the Diels–Alder reaction.[25–31] The role of the chiral cationic oxazaborolidinium catalyst **4** is investigated using the static global and local reactivity indices. The calculated values for these indices for diene **2**, dienophile **3**, and the coordination complex **3**–**4** (the *syn* coordination) are given in Table 5.

The electronic chemical potential of diene **2** is higher than that of dienophile **3** (Table 5) indicating that the charge is transferred from the diene to the dienophile along the studied Diels–Alder reaction. In addition, the electronic chemical potential difference is increased upon the coordination between dienophile **3** and catalyst **4** from 1.91 eV in the reaction between **2** and **3** to 4.98 eV in the reaction between **2** and complex **3**–**4**. Moreover, the chemical hardness of the coordination complex **3**–**4** is lower than that of dienophile **3**

Table 4. Computed Electrostatic (and Exchange) Interaction Energies (eV) for Atomic Pairs Involved in the Reaction between Diene **2** and Dienophile **3** in the Presence of Catalyst **4** along the IRC[a)]

	C_1–C_2	C_2–C_3	C_3–C_4	C_4–C_5	C_5–C_6	C_1–C_6	Total energy /eV	E_{rel} $E_{exo} - E_{endo}$ /kcal mol^{-1}
endo path								
Point (a)	−9.43	−5.35	−9.97	0.03	−8.98	−0.22	−33.92	−0.19
Point (α)	−9.12	−5.44	−9.95	−0.03	−8.64	−0.37	−33.56	2.13
TS	−8.01	−5.81	−9.52	−0.04	−7.45	−1.07	−31.89	1.11
Point (β)	−6.30	−6.55	−8.85	−0.16	−5.80	−2.60	−30.25	0.26
Point (b)	−5.82	−6.84	−8.58	−0.21	−5.39	−3.19	−30.03	−0.41
exo path								
Point (a)	−9.49	−5.34	−10.02	0.02	−8.86	−0.24	−33.93	
Point (α)	−9.20	−5.43	−9.94	0.01	−8.53	−0.38	−33.47	
TS	−8.03	−5.81	−9.56	−0.05	−7.27	−1.13	−31.84	
Point (β)	−6.33	−6.54	−8.89	−0.15	−5.67	−2.66	−30.24	
Point (b)	−5.87	−6.83	−8.62	−0.19	−5.29	−3.25	−30.05	

a) Points and carbon numbers are as illustrated in Figure 4.

Table 5. Computed Electronic Chemical Potential, μ, Chemical Hardness, η, Global Electrophilicity, ω, Local Electrophilicity, ω_k, and Local Nucleophilicity, N_k, for **2**, **3**, and complex **3**–**4**[a)]

System	μ	η	ω	ω_k				N_k	
				C_5	C_6	C_7	C_8	C_1	C_4
2	−3.30	5.77	0.94					0.39	0.28
3	−5.21	3.84	3.53	0.13	0.13	0.09	0.09		
3–**4** (*syn*)	−8.28	2.02	17.01	0.57	0.85	0.64	0.08		

a) All values are in eV. Carbon numbers are as illustrated in Figure 4.

(Table 5) (i.e., complex **3**–**4** is less resistant to charge transfer than dienophile **3**). The charge transfer is thus enhanced and leads to lowering the activation energy of the catalyzed reaction. The flow of charge from the diene to the dienophile is in agreement with the charge transfer analysis carried out at the transition state structures. As observed in Table 5, the coordination of catalyst **4** to dienophile **3** increases the electrophilicity from 3.53 to 17.01 eV rendering the coordination complex **3**–**4** a much stronger electrophile than dienophile **3**. The large increase in electrophilicity also indicates that the catalyzed Diels–Alder reaction possesses a more polar character than the uncatalyzed reaction.

Local reactivity indices are important in order to better understand the site- and regioselectivities of chemical reactions. Analysis of the local electrophilicity indices (Table 5) shows that the coordination of dienophile **3** to catalyst **4** increases the electrophilic character of the carbon atoms with C_6 being the most electrophilic position of the molecule. The electrophilicity for C_6 is higher than that for C_5 and the high asynchronicity can be described on the basis of the local electrophilicity values and can be attributed to the larger overlap between C_1 of the diene (i.e., the most nucleophilic carbon, Table 5) and C_6 of the dienophile which leads to a stronger and shorter bond.

Conclusion

The mechanism and enantioselectivity of the Diels–Alder reaction between diene **2** and dienophile **3** in the presence of organocatalyst **4** have been studied using DFT at the B3LYP/6-31G(d) level of theory. The focus of this study is mainly on the investigation and rationalization of the mechanism and enantioselectivity of the Diels–Alder reaction using various DFT-based theoretical models. These included the reaction force analysis, the natural population analysis of the charge transfer, the topological analysis of the electron localization function (ELF), the bond order analysis, and analysis based on the global and local reactivity descriptors.

The reaction force analysis and natural population analysis of the charge transfer pointed out the preference of the *endo* channel to the *exo* route for the studied Diels–Alder reaction since the former exhibited a larger charge transfer at the transition state structure which led to smaller repulsive forces that eventually resulted in activation energy lowering.

The topological analysis of the ELF provided a way for describing the breaking and formation of the bonds along the intrinsic reaction coordinate (IRC). These could be described by the disappearance and appearance of basins of attractors along the IRC. Moreover, the analysis of these basins along the IRC indicated a highly asynchronous nature of the studied Diels–Alder reaction.

The bond order and bond length analyses along the IRC also provided a tool to study the mechanism of the Diels–Alder reaction and, in agreement with the topological analysis of the ELF, indicated a highly asynchronous mechanism.

The local electrophilicity index helped to explain the high asynchronicity encountered in the catalyzed reaction and attributed it to the relatively large difference between the electrophilicity of the dienophile carbons involved in the cycloaddition reaction. The extent of the overlap between the termini carbons of the diene and the carbons of the dienophile is therefore unequal and the bond formation is asynchronous.

This study was financially supported by the Malaysian Academy of Science via SAGA Grant No. 66-02-03-0037. The authors are grateful to the Centre for Information Technology (University of Malaya) and MIMOS Berhad for providing computer facilities.

Supporting Information

Description of the numerous possible pathways for the studied reaction. This material is available free of charge on the Web at http://www.csj.jp/journals/bcsj/.

References

1 J. Sauer, R. Sustmann, *Angew. Chem., Int. Ed. Engl.* **1980**, *19*, 779.
2 K. N. Houk, J. Gonzalez, Y. Li, *Acc. Chem. Res.* **1995**, *28*, 81.
3 E. Goldstein, B. Beno, K. N. Houk, *J. Am. Chem. Soc.* **1996**, *118*, 6036.
4 K. N. Houk, B. R. Beno, M. Nendel, K. Black, H. Y. Yoo, S. Wilsey, J. K. Lee, *THEOCHEM* **1997**, *398–399*, 169.
5 D. A. Singleton, S. R. Merrigan, A. A. Thomas, *Tetrahedron Lett.* **1999**, *40*, 639.
6 A. Berkessel, H. Gröger, *Asymmetric Organocatalysis: From Biomimetic Concepts to Applications in Asymmetric Synthesis*, Wiley-VCH, Weinheim, **2005**, and references therein.
7 E. J. Corey, *Angew. Chem., Int. Ed.* **2002**, *41*, 1650.
8 E. J. Corey, *Angew. Chem., Int. Ed.* **2009**, *48*, 2100.
9 E. J. Corey, T. Shibata, T. W. Lee, *J. Am. Chem. Soc.* **2002**, *124*, 3808.
10 D. H. Ryu, T. W. Lee, E. J. Corey, *J. Am. Chem. Soc.* **2002**, *124*, 9992.
11 D. H. Ryu, E. J. Corey, *J. Am. Chem. Soc.* **2003**, *125*, 6388.
12 G. Zhou, Q.-Y. Hu, E. J. Corey, *Org. Lett.* **2003**, *5*, 3979.
13 D. H. Ryu, G. Zhou, E. J. Corey, *J. Am. Chem. Soc.* **2004**, *126*, 4800.
14 D. H. Ryu, E. J. Corey, *J. Am. Chem. Soc.* **2005**, *127*, 5384.
15 D. H. Ryu, G. Zhou, E. J. Corey, *Org. Lett.* **2005**, *7*, 1633.
16 D. Liu, E. Canales, E. J. Corey, *J. Am. Chem. Soc.* **2007**, *129*, 1498.
17 A. Ogawa, H. Fujimoto, *Tetrahedron Lett.* **2002**, *43*, 2055.
18 T. Lipińska, *Tetrahedron* **2005**, *61*, 8148.
19 R. K. Bansal, N. Gupta, S. K. Kumawat, *Tetrahedron* **2006**, *62*, 1548.
20 S. Berski, J. Andrés, B. Silvi, L. R. Domingo, *J. Phys. Chem. A* **2003**, *107*, 6014.
21 V. Polo, L. R. Domingo, J. Andrés, *J. Phys. Chem. A* **2005**, *109*, 10438.
22 L. R. Domingo, M. T. Picher, P. Arroyo, *Eur. J. Org. Chem.* **2006**, 2570.
23 E. Chamorro, R. Notario, J. C. Santos, P. Pérez, *Chem. Phys. Lett.* **2007**, *443*, 136.
24 P. Fuentealba, E. Chamorro, J. C. Santos, in *Theoretical Aspects of Chemical Reactivity*, ed. by A. Toro-Labbé, Elsevier, Amsterdam, **2007**, pp. 57–85.
25 J. Soto-Delgado, L. R. Domingo, R. Araya-Maturana, R. Contreras, *J. Phys. Org. Chem.* **2009**, *22*, 578.
26 F. Teixeira, J. E. Rodríguez-Borges, A. Melo, M. N. D. S. Cordeiro, *Chem. Phys. Lett.* **2009**, *477*, 60.
27 S. M. Mekelleche, R. Benhabib, *THEOCHEM* **2004**, *709*, 31.
28 S. Noorizadeh, H. Maihami, *THEOCHEM* **2006**, *763*, 133.
29 A. Benmeddah, S. M. Mekelleche, W. Benchouk, B. Mostefa-Kara, D. Villemin, *THEOCHEM* **2007**, *821*, 42.
30 L. R. Domingo, M. J. Aurell, M. N. Kneeteman, P. M. Mancini, *THEOCHEM* **2008**, *853*, 68.
31 J. Soto-Delgado, L. R. Domingo, R. Contreras, *THEOCHEM* **2009**, *902*, 103.
32 E. Kraka, A. Wu, D. Cremer, *J. Phys. Chem. A* **2003**, *107*, 9008.
33 H. Jiao, P. R. Schleyer, *J. Phys. Org. Chem.* **1998**, *11*, 655.
34 M.-F. Cheng, W.-K. Li, *Chem. Phys. Lett.* **2003**, *368*, 630.
35 See Supporting Information for details.
36 M. J. Frisch, G. W. Trucks, H. B. Schlegel, G. E. Scuseria, M. A. Robb, J. R. Cheeseman, J. A. Montgomery, Jr., T. Vreven, K. N. Kudin, J. C. Burant, J. M. Millam, S. S. Iyengar, J. Tomasi, V. Barone, B. Mennucci, M. Cossi, G. Scalmani, N. Rega, G. A. Petersson, H. Nakatsuji, M. Hada, M. Ehara, K. Toyota, R. Fukuda, J. Hasegawa, M. Ishida, T. Nakajima, Y. Honda, O. Kitao, H. Nakai, M. Klene, X. Li, J. E. Knox, H. P. Hratchian, J. B. Cross, V. Bakken, C. Adamo, J. Jaramillo, R. Gomperts, R. E. Stratmann, O. Yazyev, A. J. Austin, R. Cammi, C. Pomelli, J. W. Ochterski, P. Y. Ayala, K. Morokuma, G. A. Voth, P. Salvador, J. J. Dannenberg, V. G. Zakrzewski, S. Dapprich, A. D. Daniels, M. C. Strain, O. Farkas, D. K. Malick, A. D. Rabuck, K. Raghavachari, J. B. Foresman, J. V. Ortiz, Q. Cui, A. G. Baboul, S. Clifford, J. Cioslowski, B. B. Stefanov, G. Liu, A. Liashenko, P. Piskorz, I. Komaromi, R. L. Martin, D. J. Fox, T. Keith, M. A. Al-Laham, C. Y. Peng, A. Nanayakkara, M. Challacombe, P. M. W. Gill, B. Johnson, W. Chen, M. W. Wong, C. Gonzalez, J. A. Pople, *Gaussian 03 (Revision E.01)*, Gaussian, Inc., Wallingford CT, **2004**.
37 A. E. Reed, L. A. Curtiss, F. Weinhold, *Chem. Rev.* **1988**, *88*, 899.
38 F. Weinhold, in *Encyclopedia of Computational Chemistry*, ed. by P. v. R. Schleyer, John Wiley & Sons Ltd., Chichester, **1998**, Vol. 3, pp. 1792–1811.
39 K. Fukui, *Acc. Chem. Res.* **1981**, *14*, 363.
40 C. Gonzalez, H. B. Schlegel, *J. Chem. Phys.* **1989**, *90*, 2154.
41 C. Gonzalez, H. B. Schlegel, *J. Phys. Chem.* **1990**, *94*, 5523.
42 P. Fuentealba, D. Guerra, A. Savin, in *Chemical Reactivity Theory: A Density Functional View*, ed. by P. K. Chattaraj, CRC Press, Boca Raton, **2009**, pp. 281–292.
43 A. D. Becke, K. E. Edgecombe, *J. Chem. Phys.* **1990**, *92*, 5397.
44 M. Kohout, A. Savin, *Int. J. Quantum Chem.* **1996**, *60*, 875.
45 A. Savin, B. Silvi, F. Coionna, *Can. J. Chem.* **1996**, *74*, 1088.
46 M. Kohout, *DGrid, Version 4.5*, Radebeul, **2009**. The program is available by request from Dr. M. Kohout (kohout@cpfs.mpg.de).
47 I. Mayer, *Chem. Phys. Lett.* **1983**, *97*, 270; Addendum: I. Mayer, *Chem. Phys. Lett.* **1985**, *117*, 396.

48 I. Mayer, *Int. J. Quantum Chem.* **1986**, *29*, 73.
49 I. Mayer, *Int. J. Quantum Chem.* **1986**, *29*, 477.
50 I. Mayer, *J. Comput. Chem.* **2007**, *28*, 204.
51 I. Mayer, *EFF-AO, Version 1.0*, Chemical Research Center, Hungarian Academy of Sciences, Budapest, **2008**. The program is available at http://occam.chemres.hu/programs/index.html.
52 G. Lendvay, *J. Phys. Chem.* **1994**, *98*, 6098.
53 G. Lendvay, *THEOCHEM* **2000**, *501–502*, 389.
54 G. Lendvay, in *Chemical Reactivity Theory: A Density Functional View*, ed. by P. K. Chattaraj, CRC Press, Boca Raton, **2009**, p. 303.
55 R. G. Parr, L. v. Szentpály, S. Liu, *J. Am. Chem. Soc.* **1999**, *121*, 1922.
56 P. Pérez, L. R. Domingo, A. Aizman, R. Contreras, in *Theoretical Aspects of Chemical Reactivity*, ed. by A. Toro-Labbé, Elsevier, Amsterdam, **2007**, pp. 139–201.
57 L. R. Domingo, E. Chamorro, P. Pérez, *J. Org. Chem.* **2008**, *73*, 4615.
58 S. Liu, in *Chemical Reactivity Theory: A Density Functional View*, ed. by P. K. Chattaraj, CRC Press, Boca Raton, **2009**, pp. 179–192.
59 P. Pérez, L. R. Domingo, M. Duque-Noreña, E. Chamorro, *THEOCHEM* **2009**, *895*, 86.
60 E. J. Corey, T. W. Lee, *Chem. Commun.* **2001**, 1321.
61 M. D. Mackey, J. M. Goodman, *Chem. Commun.* **1997**, 2383.
62 I. Mayer, *Int. J. Quantum Chem.* **1983**, *23*, 341.